Ion Implantation Technology for Image Sensors

Nobukazu Teranishi[1, 2], Genshu Fuse[3], and Michiro Sugitani[3]
1: Laboratory of Advanced Science and Technology for Industry, University of Hyogo
1-1-2 Koto, Kamigori, Ako-gun, Hyogo 678-1205 Japan
2: Research Institute of Electronics, Shizuoka University
3-5-1 Johoku, Hamamatsu, 432-8011 Japan
3: Sumitomo Heavy Industries Ion Technology Co., Ltd. (SMIT)
1501 Imazaike, Saijo, Ehime 799-1362 Japan
E-mail:teranishi@idl.rie.shizuoka.ac.jp

Abstract Ion implantation technology is reviewed mainly from a viewpoint of image sensors, which play a significant role for implantation technology development. Image sensors are so sensitive to metal contamination that it can detect even one metal per pixel. To reduce the metal contamination, the plasma shower using RF (radio frequency) plasma generation is a representative example. The electrostatic angular energy filter after the mass analyzing magnet is a highly effective method to get rid of contamination caused by the charge exchange process. The protection layer on the silicon is needed to protect the silicon wafer against the physisorbed metals. The thickness of protection layer should be determined by considering the knock-on depth. In addition, the wafers should be cleaned up just after ion implantations and before thermal treatments. The damage by ion implantation also causes blemishes. It becomes larger in the following conditions if the other conditions are the same; a. higher energy, b. larger dose, c. smaller beam size (higher beam current density), d. longer ion beam irradiation time, e. larger ion mass. To reduce channeling, the most effective method is to choose proper tilt and twist angles. The screen oxide method is not effective because it needs a thick oxide layer. Although the pre-amorphization method is good for channeling suppression, re-crystallization quality is not yet sufficient at present. The zero-degree tilt implantation has large variation because the channeling is sensitive to even small angle variation. For P^+ pinning layer formation, the low-energy B^+ implantation method might have less metal contamination and damage, compared with the BF_2^+ method.

Keywords: image sensor, ion implantation, metal contamination, damage, channeling

1. Introduction

Solid-state image sensor technologies have been advanced drastically these 4 decades, and they brought fruitful success in the market. The sales amount on image sensors achieved 3.8 billion pieces in 2014 mainly because of the exponential growth of mobile phone market. Image sensor applications are spreading anywhere besides the mobile phones.

During the image sensor evolution, various device technologies and process technologies have been developed. Among them, ion implantation technology is one of the most important process technologies for image sensors. From the opposite viewpoint, image sensors are a very important application for ion implantation technology development; Firstly, many ion implantation steps are applied to fabricate specific structures, such as PPD (pinned photodiode) [1-3], special isolation structure [4], and to tune transistors at pixels [5]. Secondly, to obtain deep PD (photodiode), high energy implantations with a precise angle control are required, together with high aspect ratio resist patterns. In addition, a precise impurity profile formation is required to achieve a good signal electron transfer in PPD pixel. Thirdly, image sensors are very sensitive to metal contamination and crystal defects, which generate white defects (blemishes), because they have so low noise.

In this paper, ion implantation technology is reviewed mainly from a viewpoint of image sensors. First, basics of ion implantation technology are explained in Section 2. Then, metal contamination, damage and channeling, which are important topics for image sensors are discussed in Sections 3, 4 and 5, respectively. In Section 6, the P^+ pinning layer formation methods are compared.

2. Basics of ion implantation technology

Historically speaking, an ion implantation process patent was submitted by W. Shockley in 1949 [6], who is the one of the inventors of transistors. It was applied to mass-production line in early 1970's. Therefore, it can be said that it is rather a new process technology.

At first, ion implantations were used for threshold voltage control for MOS transistors. Since then, they have been adapted for various purposes;

a. Threshold voltage control.
b. High density doping, such as source-drain formation.
c. SIMOX (Separation by Implantation of Oxygen) [7].
Silicon dioxide layer is formed by oxygen implantation to obtain SOI (silicon on insulator) wafer.
d. Delamination [8].
High dose hydrogen implantation forms a delamination layer, and thin silicon layer is split at temperature above 500 °C. This phenomenon is applied to produce SOI wafers by wafer bonding method.
e. Proximity gettering [9].
Oxygen or carbon is implanted to form gettering sites nearby the front active layer. The reproducible gettering site formation is realized by the preciseness of ion implantation, and the proximity gettering is powerful because the gettering sites are nearby the front side active area.
f. Dangling bond termination [10].

Fig. 1. The rotating disk and wafer holders in the batch type ion implanters (courtesy to SMIT).

Fluorine is implanted to terminate dangling bonds. Then, interface state GR (generation recombination) centers are reduced and leakage current is decreased.

g. Amorphous formation [11].

High dose implantation forms an amorphous layer. It decreases the channeling effect, which will be explained later. It also helps re-crystallization and electrical activation during the annealing process after ion implantation.

h. Co-implantation [12].

The impurity diffusion is suppressed if dopant atoms are implanted together with carbon, nitrogen or fluorine atoms.

Focused ion beam (FIB), secondary ion mass spectroscopy (SIMS) also belongs to a category of the ion beam technology.

Ion implantation has following important features;

1) The doping amount is precise enough over 5 decades.
2) The doping area is selected by using photo-resist patterns.
3) The doping profile or depth is controlled by the ion energy.
4) Doping through a thin dielectric layer on the surface can be applied if the ion energy is appropriately selected.
5) Various species of atoms, molecules and clusters can be implanted.
6) Ion beams have sputtering effect.

Ion implanters are usually classified into three categories. The first is a medium current system mainly used for threshold voltage control and well formation. The second is a high current system mainly used for source-drain formation. The third is a high energy system used to form deep wells and PDs. From a viewpoint of wafer setting manner, there are two categories. That is, one is a single-wafer type and the other is a batch type. In the batch type, wafers are placed on a fast rotating disk, as seen in Fig. 1, in order to disperse ion beam power on multiple wafers. The batch type is mainly applied to the high current and high energy systems because they usually generate high beam power which is a product of beam energy and current.

In order to explain a typical ion implanter's structure, top view and side view block diagrams for medium-current machine, NV-MC3-II of SMIT (Sumitomo Heavy Industries Ion Technology), are shown in Fig.2 [13]. Ions are generated from a gas or solid source material at the

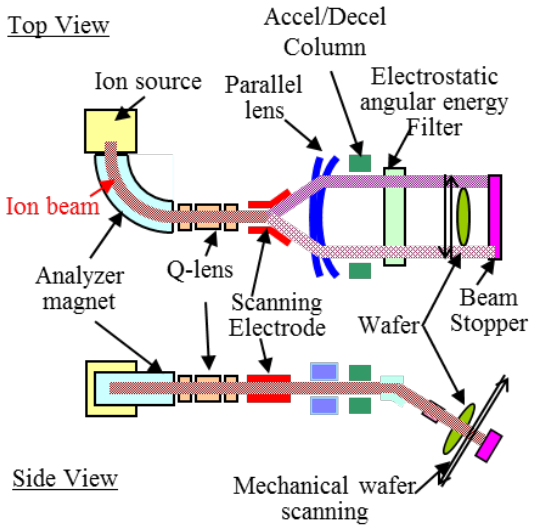

Fig. 2. The top view and side view block diagrams of medium current ion implanter, NV-MC3-II of SMIT [13].

ion source block. The generated ions are extracted by the extraction electrode, to which extraction voltage is applied, and delivered to the analyzer magnet. The analyzer magnet selects ions having a desired bending radius in the magnet, R_b, which is given as

$$R_b = \sqrt{2mV/qB^2} = p/qB \quad (1)$$

where m is ion mass, V is acceleration voltage, q is ion charge, B is magnetic flux density, and p is momentum. The Q-lens and the parallel lens shape the ion beam, and the scanning electrode block scans the ion beam to cover the entire wafer width. Next, ions are accelerated or decelerated to the desired energy at the accel/decel block if necessary. The electrostatic angular energy filter selects only the desired ions to avoid unexpected charge-exchanged ions after the analyzing magnet. Finally, they are derived into the process chamber and are implanted into the wafer. The wafer is mechanically scanned in the vertical direction perpendicular to the horizontal direction in which the ions are scanned electrically.

3. Metal contaminations

3.1. Metal contamination for image sensors

Dark current and blemish are ones of the most important and hardest problems for image sensors. There are many dark current possible causes, which are shown in a pixel cross-section of CMOS image sensor (Fig.3). One is GR centers at various locations, such as PD interface, STI (Shallow trench isolation) interface, PD depletion region, and TG (transfer gate) interface. Second is a strong electric field at the TG edge and at the junction between the P^+ pinning layer and N PD. The others are the diffusion current from the bulk, the RG (reset gate) off-leak, and charge flow from the neighbors. Ion implantation has possibility to generate GR centers by metal contaminations and crystal damages.

Dark currents for both the neutral and depleted regions are explained by using Shockley-Read-Hall (SRH) process. The recombination rate, U, is written as

$$U = \sigma v_{th} N_t \frac{pn - n_i^2}{n + p + 2n_i \cosh\left(\frac{E_t - E_i}{kT}\right)}, \qquad (2)$$

where σ is electron and hole capture cross section, v_{th} is the thermal velocity, N_t is the trap density, n_i is the intrinsic carrier density, E_t is the tarp energy level, and E_i is the intrinsic Fermi level [14]. Though the trap levels at Si-SiO_2 interface distribute widely in the bandgap, mid-gap traps with E_t=E_i contribute most as (2) shows. Therefore, it is reasonable to assume that E_t=E_i. If depleted (n, p << n_i), then, the recombination rate becomes

$$U \approx -\frac{\sigma v_{th} N_t n_i}{2\cosh\left(\frac{E_t - E_i}{kT}\right)} \approx -\frac{\sigma v_{th} N_t n_i}{2}, \qquad (3)$$

U is negative in this case and electron-hole pairs are generated. In the depleted region, generated electrons and holes drift by the electric field to the opposite directions each other. Therefore, they are not recombined, and become dark current. One GR center generates U_1;

$$U_1 = -\frac{\sigma v_{th} N_t}{2}. \qquad (4)$$

Here, it is notable that the capture cross-section, σ, depends on metal species.

Figure 4 is a dark current histogram of the virtual phase CCD [14]. It has two series of specific and periodic peaks, labeled as a and b. Four peaks for the series a are seen, and they denote 0 to 3 metal atoms at a pixel from the left to the right peak. Assuming each metal is distributed as Poisson distribution, each metal's density per pixel is derived. If the depletion region volume is estimated by the device simulation, metal density per volume can be calculated. The σ is derived from the peak pitch using (4). The obtained metal densities and σ's are shown in the inset table. The metal is identified from its cross-section. This method is called dark current spectroscopy [14].

As explained above, image sensors are so sensitive to metal contaminations that even one metal atom can make a blemish.

3.2. Metal contamination classification

Figure 5 shows examples of metal contamination measurement by ICPMS (inductively coupled plasma mass spectrometry) [16]. The samples are about 1 μm thick surface layer, which are implanted by 2E16 cm^{-2} arsenic (As) with 80 keV energy. Red and blue bars denote the metal contamination before and after a new countermeasure for reduction of metal contamination applied to MC3-II of SMIT, respectively. Although the metal contamination is much improved by the new countermeasure, metals, such as Al, Cr, Cu, Fe, Ni, Ti, and W, were still detected. Therefore, it is important to clean implanters more and in parallel to develop design and process flow, which are proof against metal contaminations.

Metal contaminations through ion implantation are classified into two categories; one is energetic metal ion and the other is physisorption. Figure 6 shows cross

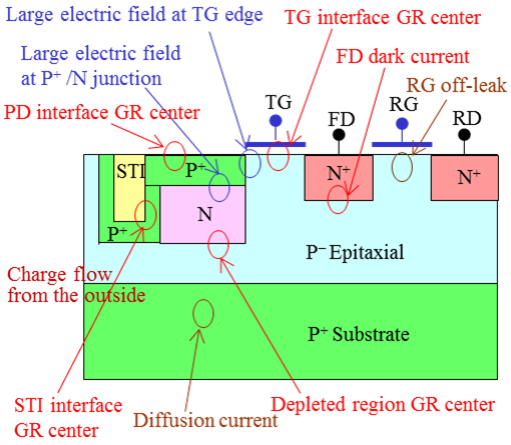

Fig. 3. Various possible causes of dark current generation, illustrated in CMOS image sensor pixel cross-section. PD: photodiode, TG: transfer gate, FD: floating diffusion, RG: reset gate, RD: reset drain, GR center: generation recombination center, STI: shallow trench isolation.

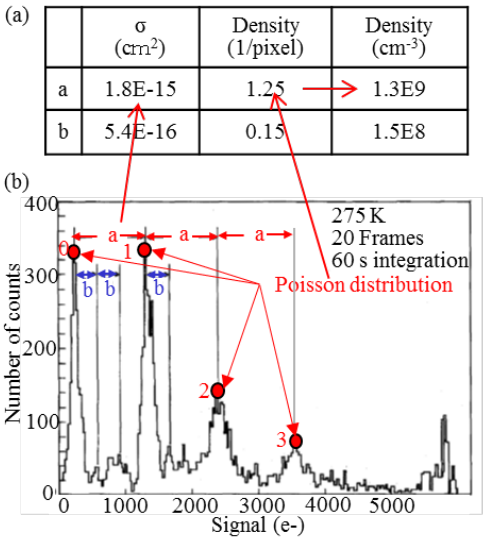

Fig. 4. Dark current spectroscopy [15].
(a) Obtained capture cross sections and metal densities.
(b) Dark current histogram, having two series of specific and periodic peaks, labeled as a and b.

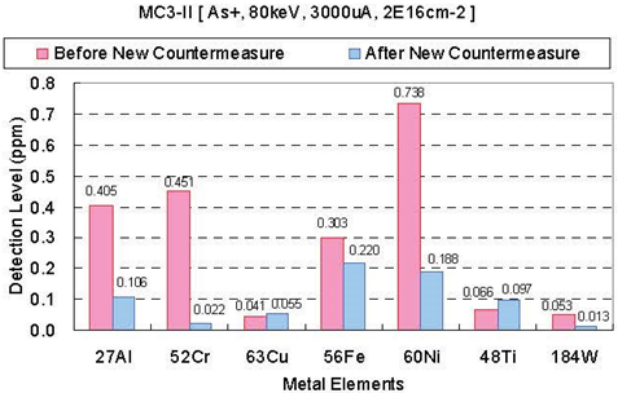

Fig. 5. Metal contamination measurement by ICPMS [16]. Red denotes the metal contamination before the new countermeasure, and blue denotes that after the new countermeasure, MC3-II of SMIT.

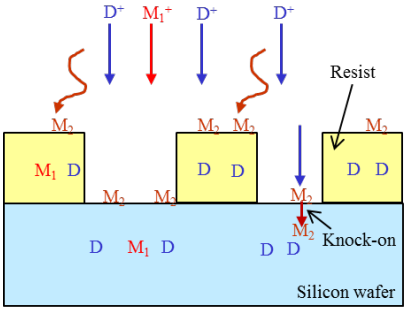

Fig. 6. Cross sectional illustration showing ion implantation process and metal contaminations. Straight line arrows denote energetic ion implantation, and wiggle line arrows denotes physisorption. D: dopant, M_1: metal, which is implanted, M_2: metal, which is physisorped.

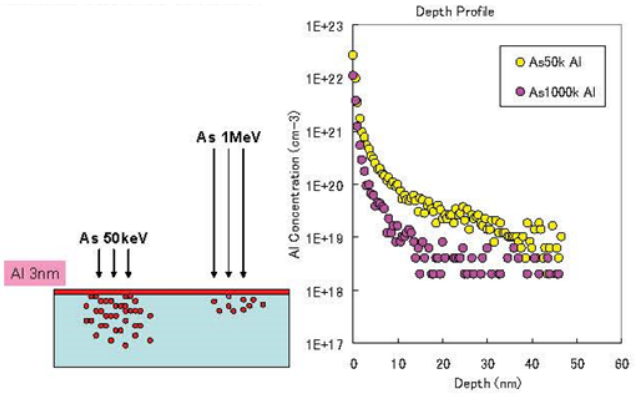

Fig. 7. An example of knock-on effect [16].
(a) Illustration showing the simulation condition.
(b) Knocked-on aluminum depth profiles by Monte Carlo simulation.

sectional illustration showing ion implantation process and metal contaminations. Straight line arrows denote energetic ion implantation, and wiggle line arrows denote physisorption. Here, D is a dopant and M_1^+ is a metal ion, which has energy and impinges to the wafer together with the dopants. M_2 denotes another metal atom/ion, which has a small (thermal) energy and is physisorbed on the wafer surface.

3.3. Physisorption metal contamination

Although most of the physisorbed metals are washed out by a following cleaning process, some of them invade into silicon by thermal diffusion or knock-on. Figure 7 shows the knocked-on aluminum depth profiles by Monte Carlo simulation [16]. The condition is that after a 3 nm thick aluminum layer is deposited on the silicon wafer, 1E15 cm^{-2} As with two different energies, 50 keV and 1 MeV, is implanted. The depth profile becomes larger and deeper if the implantation energy is smaller. While the knocked-on aluminums reach 15 nm deep in silicon by 1 MeV, they reach 45 nm deep in silicon by50 keV. It is notable that if the ion energy is smaller, the knock-on becomes larger because the cross section becomes larger.

There are two important cautions to avoid the physisorption metal contamination; (a) A protection layer, typically thin silicon dioxide layer, should be placed on the wafer during ion implantation. The thickness of the

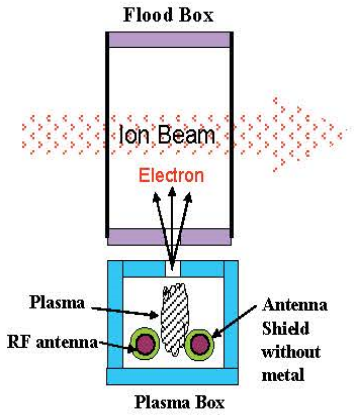

Fig. 8. Illustration of plasma shower using RF (radio frequency) plasma generation [16].

protection layer should be determined by considering the knock-on depth. If the temperature during the ion implantation is high, the thermal diffusion length of metals should be considered. (b) The wafers should be cleaned up just after the ion implantations and before the thermal treatments. It is effective if the protection layer is etched even in a little amount during the cleaning.

3.4. Contamination reduction in implanters

To reduce metal contamination, various technologies have been developed for ion implanters. A couple of them will be explained in this subsection.

One is an ion beam neutralizer, which is applied to suppress the chargeup. In the early stage, electron shower was used, which generates primary electrons by hot metal filament and accelerated electrons are hit on an aluminum plate to generate secondary electrons. These secondary electrons neutralize ion beam and wafer surface. Its drawback is metal contamination and rather high energy of the secondary electrons. To eliminate these drawbacks, plasma shower was developed and has been used. As illustrated in Fig. 8 [16], plasma is generated by hot filament or radio frequency (RF) antenna in plasma box, and electrons are extracted to the flood box. Then, they neutralize the ion beam and wafer surface. Because plasma is used, the energy of the extracted electrons is small, which is good for neutralization. When RF antenna, coated with non-metal dielectric material, is used, metal contamination is much reduced.

Another is an energetic metal ion contamination in case of BF_2^+ implantation. If the magnetic bending radius of some ion equals to that of $^{11}BF_2^+$ (shortly, R_b (some ion) = R_b ($^{11}BF_2^+$)), the ion can pass through the analyzer magnet, and becomes energetic metal ion contamination. When the ion source arc chamber is made of molybdenum (Mo), Mo contamination occurs because R_b ($^{98}Mo^{++}$) is exactly equal to R_b ($^{11}BF_2^+$) [17]. When the ion source arc chamber is made of tungsten (W) or because W is usually used as a filament or cathode material in the ion source, wafers can be contaminated by W. The mechanism of W contamination is not so simple as the Mo case described above. Alternatively, charge exchange and/or molecule decomposition models were introduced for $^{184}W^{19}F^{++}$ [18] and $^{184}W^{12}C^+$ [19] extraction. At this moment it cannot be determined which mechanism is more realistic, but at

least it is true that arc chamber material change from W to carbon (C) reduced W contamination only to half [18], which means that the effect of filament material still remains or some components other than ion source should be considered as origins of contamination.

The electrostatic angular energy filter shown in Fig. 2 after the mass analyzing magnet is a highly effective method to get rid of both contaminations caused by the charge exchange process and off-energy ions. This is because a magnet analyzer acts as a filter of momentum per charge and an electrostatic filter selects energy per charge. If the final energy filter is utilized by a magnetic field, such a filtering ability cannot be expected. [19].

4. Damages

Since the energy of ion implantation is several orders of magnitude higher than the binding energy of silicon, it generates damages (crystal defects), including vacancies, interstitials and finally an amorphous layer. After ion implantation, annealing is carried out to restore the silicon crystallinity and to activate dopants electrically. The residual defects have serious effects to following processes and device performances. One important example for processes is that diffusion constants are changed due to the defects, especially vacancies and interstitials. Therefore, even if dopant profiles are the same just after the implantation, if damages are different, the final dopant profiles usually become different. Image sensors suffer from dark current increase and blemishes. In this section, damages by ion implantations will be discussed.

First, damages are compared between the single-wafer type, MC3 of SMIT, and the batch type, GSD-HE of SMIT, in Fig. 9. To measure damages, therma wave (TW) is used, which has positive relation with the damage. The implantation condition is P^+, 90 keV, 2E13 cm^{-2}. In GSD-HE, 13 200-mm wafers are loaded at once. Both of the single-wafer type and the batch type have larger TW value or larger damage when the beam current density increases in a range from 20 to 200 μA/cm^2. This is reasonable result. The single-wafer type has larger TW value compared with the batch type. The TW value of the single-wafer type at 40 μA/cm^2 is equal to that of the batch type at 200 μA/cm^2. It can be said that batch type has effectively 1/5 of the ion beam current density of the single-wafer type from a damage viewpoint.

Figure 10 illustrates the damage distributions on a wafer for the two types. The damage uniformity of the batch type is better together with the damage level. In case of the single-wafer type, the left hand side and the right hand side have larger damage. It is because the ion beam turns back at left hand side and right hand side, and then the beam irradiation period becomes longer and/or interval becomes shorter at the both sides. The batch type has a little damage non-uniformity, where the damage at the disk inner side is larger than that at the disk outer side.

This damage non-uniformity at the batch type is explained using another experimental result in Fig. 11 and 12 [21]. Figure 11 shows the configuration of the disk, the wafer and the beam spots. The distances from the disk center are 71 cm at the disk outer side, 61 cm at the wafer center, and 51 cm at the disk inner side. Since the disk

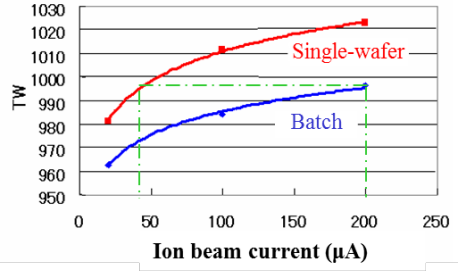

Fig. 9. Therma wave (TW) value comparison between the single-wafer type and the batch type implanters[20].
Single-wafer type: MC3 (SMIT), Batch type: GSD-HE (SMIT).
Ion: P^+, Energy: 90 keV, Dose: 2E13 cm^{-2}.

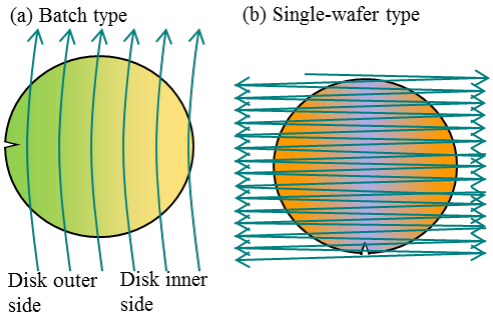

Fig. 10. Damage distribution illustrations [16].
Arrows denote beam scans.
(a) Batch type: The damage is smaller and more uniform. The damage at the disk inner side is slightly larger.
(b) Single-wafer type: The damage at the left side and the right side is largest.

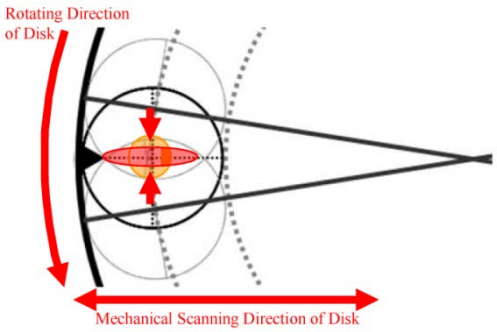

Fig. 11. Configuration of the disk, the wafer and the beam spots [21].
Two kinds of beam spot shapes are prepared;
Round shape: Reference,
Oval shape: To shorten the beam irradiation time.

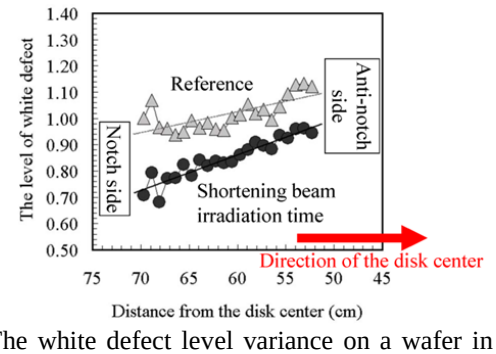

Fig. 12. The white defect level variance on a wafer in a CCD image sensor [21].

spinning speed is 815 rpm, the beam moving speeds on the wafer are 6.1 cm/ms at the disk outer side, 5.2 cm/ms at the wafer center, and 4.4 cm/ms at the disk inner side. Therefore, the beam moving speed at the disk inner side is 1.4 times slower than that at the disk outer side. Two kinds of beam spot shapes are prepared; one is a conventional round shape and an oval shape, which shortens the beam irradiation time. Figure 12 shows the level of white defects in a CCD image sensor. The horizontal axis is the position from the disk center. The disk inner side has a smaller number, while the disk outer side has a larger number. The vertical axis is the relative level of white defects. This result clearly shows that the damage at the disk inner side is larger, and the damage of the oval beam shape is smaller. Another experimental result is shown in Fig. 13, which is the disk spinning speed dependence of the damage layer thickness. Although an amorphous layer was not generated by this experiment, a damage layer with different optical index was observed by a spectroscopic ellipsometer. As shown in Fig. 13, the damage layer is smaller, when the disk spinning speed is larger. Even if the damage becomes smaller, the resist pattern breakage by particles might become more frequent. The results, as shown in Fig. 9-13, suggest that even if the dose amounts and beam currents are the same, shorter irradiation time case shows smaller damage.

Next, mass effect will be discussed. Table 1 shows the amorphous layer thickness by As dimer implantation, compared with that by As monomer implantation [20]. The energy for As dimer is set to be twice larger than that for the monomer, and the dose is set to be half of that for the monomer to keep the equivalence. The amorphous thicknesses for the dimer are larger than those for the monomer, as shown in Table 1. Another fact is that BF_2^+ implantation with 1E15 cm^{-2} dose usually generates amorphous layer, while the 1E15 cm^{-2} B^+ implantation, accompanied by the 2 E15 cm^{-2} F^+ implantation, dose not generate any amorphous layer [20]. Both results imply that larger ion mass makes larger damage.

It can be said that the ion implantation damages become larger as the following conditions if other conditions are the same;

a. Higher energy.
b. Larger dose.
c. Higher beam current density.
d. Longer ion beam irradiation time.
The higher disk spinning speed has smaller damage in the batch type.
e. Shorter ion beam irradiation interval
The damage by batch type is smaller than that by single-wafer type.
f. Larger ion mass.

5. Channeling

Because image sensors have low noise, even small irregularities are not allowed. One of the important problems is image lag in the PPD [22]. No single signal electron should not be remained in the PD after the transfer period. Therefore, in order to realize no image lag, precise design and process technology should be applied to form PPD pixels. As explained in Section 2, ion

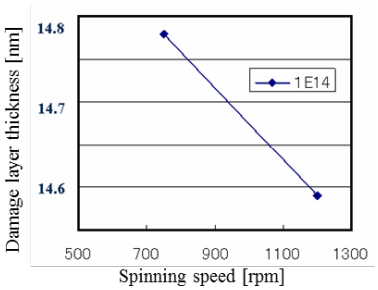

Fig. 13. Damage layer thickness dependence disk spinning speed [20].
Batch type: GSD-HE (SMIT), Ion: BF_2, Energy: 20 keV, Dose: 1E14 cm^{-2},
Although amorphous layer was not generated by this experiment, a damage layer with different optical index was observed by a spectroscopic ellipsometer. The damage layer thickness indicates thickness of the damage layer, measured by the spectroscopic ellipsometer

Table 1. The amorphous layer thickness by As dimer implantation, compared with that by As monomer implantation [20].

Ion	Energy	Dose	Amorphous thickness
	(keV)	(cm-2)	(nm)
As^+	15	3.0E+14	25.5
			∧
As_2^+	30	1.5E+14	26.4
As^+	15	1.0E+14	21.3
			∧
As_2^+	30	5.0E+13	22.2

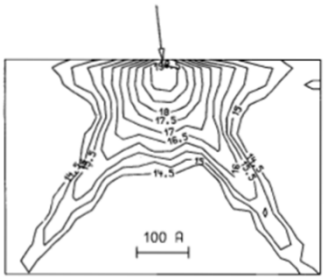

Fig. 14. Boron concentration profile of point response by Monte Carlo simulation [23].
Wafer: (100), Ion: B^+, Energy: 0.5 keV, Dose: 1E15 cm^{-2}, Tilt: 7 º, Twist: 22 º.
The arrow denotes the point, where B^+ is implanted.

implantation can afford precise dose, depth and doping area. However, it has a large limitation, i.e., channeling. Figure 14 shows the boron concentration profile by Monte Carlo simulation as an extreme example [23]. The arrow denotes the point, where B^+ ions are implanted with the conditions; (100) silicon wafer, 0.5 keV energy, 1E15 cm^{-2} dose, and 7° tilt, 22° twist. This combination of the angles is regarded as a small channeling condition. However, because ion energy is so small and channeling becomes so large that the profile is much different from

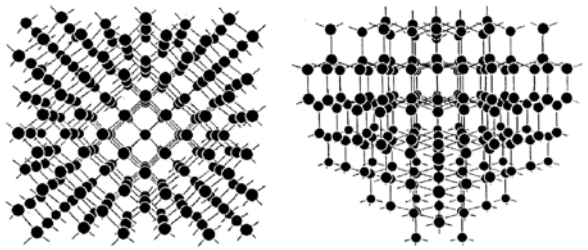

(A) Axial channeling (B) Planar channeling.

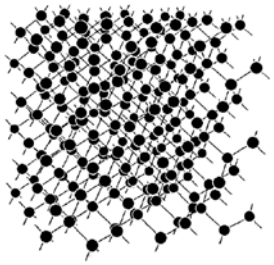

(C) No channeling (Random arrangement).

Fig. 15. Illustrations to show the appearance difference of crystal lattice by the view angle [24].

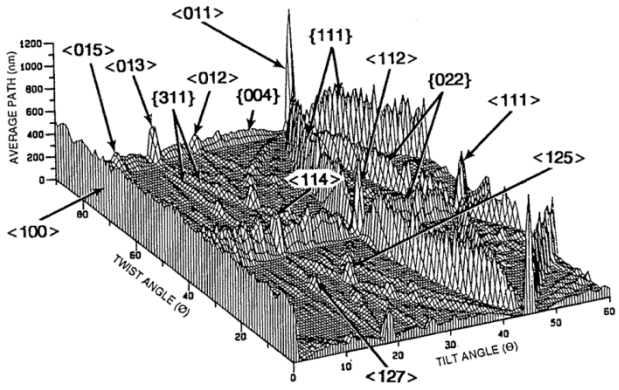

Fig. 16. Average path dependence on the tilt and twist angles by Monte Carlo simulation [25-27].
The mean path is the distance along the ion trajectory until its direction deviates by more than 2º from the initial incident direction.
Ion: B^+, Energy: 100 keV, Tilt pitch: 1º,
Twist pitch: 2º, Number of average: 200.
The notch position is at twist =45º.

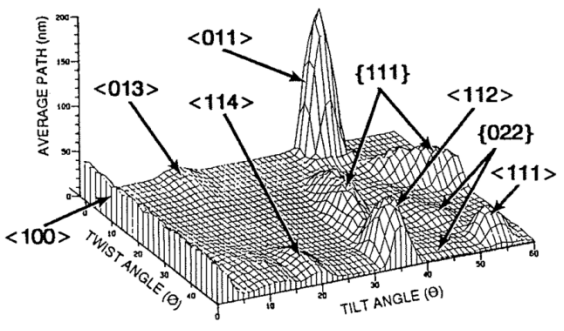

Fig. 17. Average path dependence on the tilt and twist angles by Monte Carlo simulation [25-27].
The mean path is the distance along the ion trajectory until its direction deviates by more than 4º from the initial incident direction.
Ion: B^+, Energy: 5 keV, Tilt pitch: 1º,
Twist pitch: 2º, Number of average: 200.

those obtained by usual process simulators. Notable fingers are formed in <110> direction due to de-channeling. Channeling brings a deeper dopant profile, which causes lower sheet resistance. It also wreaks undesirable dopant distribution dependence on channeling direction, sheet resistivity non-uniformity on a wafer, lot-to-lot sheet resistivity variation. Moreover, it might bring unexpected electric field concentrations at the fingertips. In this session, channeling will be discussed.

Figure 15 illustrates the appearance difference of crystal lattice by the view angle. There are pipe-like spaces (channels) in (A) and sheet-like spaces in (B), while there are no spaces in (C), which looks like a random arrangement. If ions fly through these spaces with little collisions, it is called channeling. There are two kinds of channeling; one is axial channeling (A) and the other is planar channeling (B).

The channeling depends on the silicon surface orientation, the ion beam angle, energy, ion species, substrate temperature, etc. Figure 16 shows the average path dependence on the tilt and twist angles by Monte Carlo simulation [25-27]. The mean path is defined as the distance along the ion trajectory until its direction deviates by more than 2° from the initial incident direction. The average path is an average over 200 simulated paths. The notch is located at twist = 45°. The mountain ranges indicate the planner channeling, and the independent peaks are the axial channeling. There are so many axial and planner channeling directions. Among them, <011> axial is the largest. Other prominent axial channels are <112>, <100>, <111>, <013>, and <114>. Planar channels are apparent for {111}, {022}, {311}, and {004}. The preferable tilt and twist combinations to reduce channeling can be chosen by using Fig. 15. Because the wafer orientation and implanter angel setting have errors and ion directions are changed in the silicon by the error, they needs some margin. If the ion implantation direction has some angle to TG to suppress the channeling, for example, multi-step implantation should be applied to keep the symmetry.

Figure 17 shows the average path dependence on the tilt and twist angles with 5 keV energy. The average path becomes smaller and the peaks and mountain ranges becomes broader compared with 100 keV energy case. Because the average path is the integration from the initial energy to zero, it becomes larger when the energy is larger. However, because the ratio of the average path to the range becomes larger when the energy becomes smaller, it can be said that the channeling is larger when the energy is smaller. Actually, most severe problem for channelings is the tailing of the doping profile, which is determined by the final stage of ion trajectory.

To reduce channeling, there are the screen oxide method and amorphization method other than the beam direction selection. Figure 18 shows the effect of the screen oxide. 150 keV, 4E13 cm^{-2}, $^{11}B^+$ is implanted into (100) silicon wafer. The screen dioxide thicknesses are 7.6 nm, 33.6 nm and 101.5 nm. Because silicon dioxide is amorphous and the ion directions are scattered, the channeling becomes smaller as the screen dioxide becomes thicker. However, if the required screen oxide thickness is too large, the screen oxide method is not

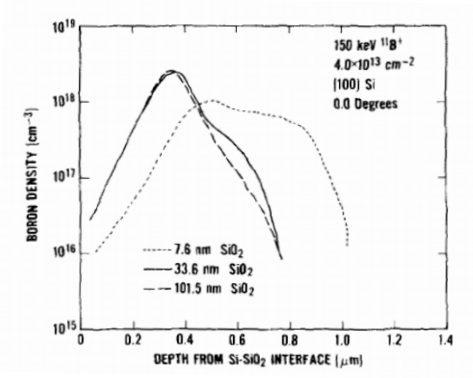

Fig. 18. Boron density profile with various screen oxide thickness [28]
Wafer: (100) Silicon, Ion: $^{11}B^+$, Energy: 150 keV, Dose: 4E13 cm^{-2}, Tilt: 0.0 $\pm$ 0.1°

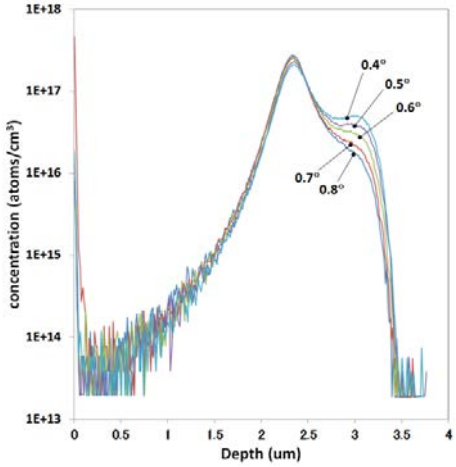

Fig. 19. SIMS profiles implanted in 0.1° tilt steps [29].
Ion: B^+, Energy: 1,500keV, Dose: 1E13 cm^{-2}, Tilt: 0.4 – 0.8°

practical for the latest fine technology. As explained in Section 4, the amorphous layer is generated by high dose and larger mass ion implantation. This amorphous layer reduces channeling. For example, the sheet resistance uniformity at 5E15 cm^{-2} dose, 50 keV energy, 7° tilt of P^+ implantation is much better than that at 1E13 cm^{-2} dose implantation [28]. However, even in this case, part of ions are implanted with the channeling condition before the amorphous layer is formed. Additionally, smaller mass ions do not generate amorphous layer. In order to suppress the channeling even in these conditions, the pre-amorphization method is introduced [11]. Electrically-neutral ions, such as Ge or Si, are implanted at a high-dose beforehand to form an amorphous layer. Then, electrically-active ions, such as B, are implanted without suffering from channeling. Finally, the amorphous layer is re-crystalized by the following annealing. On the other hand, even though a fine logic process uses this method, image sensors are so sensitive that there is still a room for improvement on the re-crystallization quality in this method at present.

Lastly, discussion is focused on zero-degree tilt implantation, which is applied to avoid shadowing occurring due to resist patterns and to obtain deeper profiles by intentional channeling. Figure 19 shows the SIMS profiles implanted with 0.4 - 0.8° tilts in 0.1° steps,

Table 2. Comparison between B^+ and BF_2^+ implantations for forming P^+ pinning layer at PPD.
Note 1) High-current low energy implanters are assumed, such as SHX series of SMIT, which has 200 eV minimum energy [16].
2) Knock-on effect is smaller because the mass of $^{11}B^+$ is 11/49 times smaller than that of $^{11}B^{19}F_2^+$.
3) Smaller sputtering effect and energetic metal contamination.
4) F^+ can be implanted separately if needed.

	Low energy B^+ 1)	BF_2^+
Productivity	Same	
Shallow depth	Same	
Lateral spread	Same	
Damage	Advantage 2)	
Metal contamination	Advantage 3)	
Fluorine effect	Separate F^+ implantation 4)	Advantage in some cases

1,500 keV energy, 1E13 cm^{-2} dose of B^+ [29]. There are clear differences in the SIMS profile even only 0.1° tilt steps due to the channeling differences. Because the wafer orientation and implanter angle setting contain errors, it is difficult to control channeling at present. Therefore, it can be said that the zero-degree tilt implantation is quite variable process.

6. B vs. BF_2 for PPD formation

One of the critical implantations is that to form the P^+ pinning layer of PPD, which affects both the complete signal electron transfer from PD to FD through TG and the dark current / blemishes. If the P^+ pinning layer is thicker, the signal electron transfer becomes difficult. Its edge position with reference to the TG gate edge is also a sensitive parameter. To reduce dark current and blemishes, metal-free is required because the electric field between the P^+ pinning layer and N PD is large, as shown in Fig.3.

There are two options for this implantation, i.e., low-energy B^+ or BF_2^+ implantations. Table 2 shows the comparison between them. High-current low energy implanters are preferable for the low-energy and medium-dose B^+ implantation, such as SHX series of SMIT, which can provide 200 eV as the minimum energy [16]. Then, the productivity is same even in case of the strong deceleration mode. Doping profiles, including the depth and lateral spread of the two conditions are almost in the same levels. The low-energy B^+ generates smaller damage because a mass of $^{11}B^+$ is 11/49 times smaller than that of $^{11}B^{19}F_2^+$. Metal contamination of the low-energy B^+ is also less thanks to a smaller knock-on and sputtering effect and less energetic metallic ions, as explained in Subsection 3.4. Fluorine from BF_2 has a positive effect for dark current reduction on a case-by-case basis because fluorine can terminate the dangling bonds. In case of low-energy B^+, F^+ can be implanted separately if necessary.

Since the formation of the N PD and the P^+ pinning layer are complicated in practice, the selection is not straightforward. Simply speaking, the low-energy B^+ looks better.

7. Conclusions

Ion implantation is an indispensable technology for image sensors, and image sensors play a significant role for implantation technology development.

Image sensors are so sensitive to metal contamination that dark current spectroscopy can detect only one metal per pixel. Image sensors have been always requiring metal contamination reduction of ion implanters. The plasma shower using RF plasma generation is a representative example. Although some metal ions, such as $^{184}W^{19}F^{++}$ [18] and $^{184}W^{12}C^+$, cannot be removed by the mass analyzing magnet due to the charge exchange process, the electrostatic angular energy filter after the mass analyzing magnet is a highly effective method to get rid of such contamination caused by the charge exchange process. The protection layer on the silicon is needed to protect the silicon wafer against the physisorbed metals. The thickness of the protection layer should be determined by considering the knock-on depth. In addition, the wafers should be cleaned up just after ion implantations and before thermal treatments.

Crystal damage by ion implantation also causes blemishes. The damage becomes larger as the following conditions if the other conditions are the same; a. Higher energy. b. Larger dose. c. Higher beam current density. d. Longer ion beam irradiation time. e. Shorter ion beam irradiation interval. f. Larger ion mass.

To obtain precise doping profiles, channeling should be reduced. The most effective method is to choose proper tilt and twist angles. If ion implantation direction has some angle to TG to suppress the channeling, for example, multi-step implantation should be applied to keep the symmetry. The screen oxide method is not effective because it needs thick oxide layers. Although the pre-amorphization method is good for channeling suppression, re-crystallization quality is not yet sufficient at present. The zero-degree tilt implantation has large variation because the channeling is sensitive to even small angle variation, especially in a high-energy case.

For P^+ pinning layer formation, the low-energy B^+ implantation method might have less metal contamination and damage, compared with the BF_2^+ method.

There remain important topics on ion implantation relating to image sensor fabrication, which are not discussed in this paper, such as annealing, high energy implantation, trench implantation, uniformity, and so on.

References

[1] N. Teranishi, A. Kohono, Y. Ishihara, E. Oda, K. Arai: “No Image Lag Photodiode Structure in the Interline CCD Image Sensor," IEEE IEDM, pp.324-327, 1982.

[2] E. R. Fossum and D. B. Hondongwa: “A Review of the Pinned Photodiode for CCD and CMOS Image Sensors,” IEEE J Electron Devices Soc., vol.2, no. 3, pp.33-43.

[3] N. Teranishi, “Effect and Limitation of Pinned Photodiode,” IEEE Transaction on Electron Devices, vol. 63, no. 1, pp. 10-15, 2016.

[4] K. Itonaga, K. Mizuta, T. Kataoka, M. Yanagita, H. Ikeda, H. Ishiwata, Y. Tanaka, T. Wakano, Y. Matoba, T. Oishi, R. Yamamoto, S. Arakawa, J. Komachi, M. Katsumata, S. Watanabe, S. Saito, T. Haruta, S. Matsumoto, K. Ohno, T. Ezaki, T. Nagano, and T. Hirayama: "Extremely-Low-Noise CMOS Image Sensor with High Saturation Capacity", IEEE IEDM, 8.1, pp.171-174, 2011.

[5] X-Y. Wang, M. F. Snoeij, P. R. Rao, A. Mierop, A. J.P. Theuwissen, “A CMOS Image Sensor with a Buried-Channel Source Follower,” IEEE ISSCC, 2.10, pp.62-63, San Francisco, USA, Feb. 2008.

[6] W. Shockley; “Semiconductor Translating Device,” US Patent 2,666,814, applied on April 27, 1949.

[7] K. Izumi, M. Doken and H. Ariyoshi; “CMOS Devices Fabricated by SiO_2 Layers formed by Oxygen Implantation into Silicon,” Electonics Letters, vol.14,no.18, p.593-294, 1978.

[8] T. Hara, K. Kajiyama, T. Yoneda and M. Inoue; “Delaminations of Thin Layers by High Dose Hydrogen Ion Implantation in Silicon,” J. Electrochemical Society, vol.143, no.8, pp.L166-L168, 1996.

[9] H. Wong, N. W Cheung, P. K. Chu, J. Liu, and J. W. Mayer, “Proximity gettering with mega-electron-volt carbon and oxygen implantations,” Applied Physics Letters, vol.52, no.12, pp.2555-2557, 1987.

[10] K. Ohyu, T. Itoga and N. Natsuaki; "Advantages of Fluorine Introduction in Boron Implanted Shallow p+/n-Junction Formation," Japanese J. Applied Physics, vol.29, no.3, p.457-462, 1990.

[11] D.K. Sadana, E. Myers, J. Liu, T. Finstad and G.A. Rozgonyi; “Germanium Implantation into Silicon An Alternate Pre‐Amorphization/Rapid Thermal Annealing Procedure for Shallow Junction Formation,” J. Electrochemical Society, vol.131,no.4, pp.943-945, 1984.

[12] A. Vanderpool; “Importance of the Carbon Kick-out Mechanism in Reducing Transient Enhanced Diffusion,” Proc. 17th Int. Conf. Ion Implantation Technology, pp.213-216, 2008.

[13] M. Sugitani, F. Sato, M. Koike, M. Sano, and K. Ueno; “Introduction of the MC3-II/WR System, an Extended Energy Medium Current Ion Implanter,” Proc. 17th Int. Conf. Ion Implantation Technology, pp.269-272, 2008.

[14] S. M. Sze, Physics of semiconductor devices 2nd Edition, John Wiley & Sons, 1981, ch. 1, pp. 35-38, Eq. 59 and ch. 2, pp. 84-89.

[15] R. D. McGrath, J. Doty, G. Lupino, G. Ricker, and J. Vallerga; “Counting of Deep-Level Traps Using a Charge-Coupled Devices,” IEEE Transaction on Electron Devices, vol.ED-34, no.12, pp.2555-2557, 1987.

[16] G. Fuse and M. Sugitani; “Fundamental Ion Implantation Technologies for Image Sensor Devices,” Proc Int. Image Sensors Workshop (IISW), pp.17-20, Snowbird, USA, June 2013.

[17] A. Cubina and M. Frost; “Effect of Molybdenum Contamination Resulting from BF_2 Implantation,” Nuclear Instrument and Methods in Physics Research, vol.B55, pp.160-165, 1991.

[18] R. B. Liebert, G. C. Angel and M. Kase; “Tungsten Contamination in BF_2 Implants,” Proc. 11th Int. Conf. Ion Implantation Technology, pp.135-138, 1996.

[19] G. Fuse and M. Sugitani; “Fundamentals of Ion Implantation Technologies for Image Sensing Devices,” ECS Transactions, vol.60, no.1, pp.675-680, 2014.

[20] G. Fuse, M. Sano, H. Murooka, T. Yagita, M. Kabasawa, T. Shiraishi, Y. Fujino, N. Suetsugu, H. Kariya, H. Izutani, and M. Sugitani; “Electrical Characteristics Due to Differences in Crystal Damage Induced by Various Implant Conditions,” Nuclear Instruments and Methods in Physics Research, vol.B237, pp.77-80, 2005.

[21] E. Kanazaki, N. Iwawaki, F. Kawase, and S. Shibata; “Implant Damage Evaluation at High Energy and Low Dose Ion Implantation Using White Defect of CCD Image Sensor,” Ext. Abs. 9th Int. Workshop on Junction Technology, S6.6, pp.106-109, Kyoto, Japan, June 2009.

[22] N. Teranishi; “The Pinned Photodiode,” Workshop on CMOS Image Sensors for High Performance Applications, Toulouse, France, November 2015.

[23] G. Hobler, H.-H. Vuong, J. Bevk, A. Agarwal, H. –J. Gossmann, D. C. Jacobson, M. Foad, A. Murrel,l and Y. Erokhim; “Modeling of Ultra-Low energy Boron Implantation in Silicon,” IEEE IEDM, 19.1.1, pp.489-492, 1997.

[24] G. Fuse and T. Hirao; “Ion Implantation Technology has come to this point ! ”, Kogyo Chosakai Publishing Co.,Ltd., Tokyo, Japan, 1991, [in Japanese].

[25] R. F. Lever and K. W. Brannon; “A low Energy Limit to Boron Channeling in Silicon,” J. Applied Physics, vo.69, pp.6369-6372, 1991.

[26] R. F. Lever and K. W. Brannon; “Crystallographic Aspects of Low Energy Boron Implantation into Silicon,” Material Research Society Symp. Proc., vol.100, pp.249-254, 1988.

[27] R. Simonton and L. Rubin; “Channeling Effects in Ion Implantation into Silicon,” in “Handbook of ION IMPLANTATION TECHNOLOGY" edited by J, F. Ziegler, North-Holland, pp.303-340, 2002.

[28] D. R. Myers, J. Comas, R. G. Wilson; “Effect of Silicon Dioxide Surface‐Layer Thickness on Boron Profiles for Directly Aligned Implants into (100) Silicon,” J. Applied Physics, vol.52, no.5, pp.3357-3359, 1981.

[29] K. Watanabe, H. Sasaki, M. Kabasawa, M. Tsukihara, and K. Ueno; “Introduction of the S-UHE, a Single-Wafer Ultra-High Energy Ion Implanter,” Proc. 20th Int. conf. Ion Implantation Technology, 26 June – 4 July 2014.